# Health Monitoring of Rail Structures Using Guided Waves and Three-dimensional Diagnostic Imaging

Chao ZHOU [1], Chunliang ZHANG [1, †], Zhongqing SU [2], Xia YUE [1], Jianhua XIANG [1] and Guiyun LIU [1]

[1] School of Mechanical and Electric Engineering, Guangzhou University, Guangzhou, Guangdong Province 510006, PR China

[2] The Department of Mechanical Engineering, The Hong Kong Polytechnic University, Kowloon, Hong Kong SAR

**Submitted to *Structural Control and Health Monitoring***

(revised in October, 2016)

[†] To whom all correspondence should be addressed

Email: nhzcl@163.com (Prof. Chunliang Zhang, Ph.D.), Fax : +86-20-39366928

**Abstract**

With the rapid development of high-speed railway around the world, more advanced nondestructive evaluation (NDE) and structural health monitoring (SHM) techniques are required to detect structural damage in its forming stage before the damage jeopardizes the safety of the structures. In this aspect, guided-wave-based diagnostic imaging is a recent research focus, aimed at intuitionally showing the healthy status of the structure under inspection. However, the present diagnostic imaging techniques are mostly two-dimensional imaging methods which fail to inspect complicated solid structures. In this study, a novel three-dimensional diagnostic imaging technique was developed in conjunction with an active sensor network, capable of real-time monitoring complex solid engineering structures. The ToF-based signal features were extracted from captured guided waves signals, and subsequently applied to define field values. The effectiveness of the approach was examined by identifying a crack introduced into a part of the real rail structure using both FE simulation and experiments. Results have revealed that the developed three-dimensional imaging approach is able to quantitatively visualising structural damage in complicated solid engineering structures.

***Keywords*****:** guided waves, three-dimensional diagnostic imaging, rail structure, structural health monitoring

## 1. Introduction

Nondestructive evaluation (NDE) of high speed railway has become a significant problem around the world [1]. Operating in very high speed (350 km/h), the railway track structures are prone to various types of damage, especially for the fatigue cracks, potentially leading to catastrophic failure. Traditional NDE techniques (*e.g.* ultrasonic scanning, eddy current, radiography and magnetic particle testing) require downtime to perform scheduled tests during the lifespan. Moreover, for some large structures (*e.g.* high speed train and airplane), disassembly of some key components is required, which is costly and sometimes impractical. Envisaging such deficiencies, structural health monitoring (SHM) has emerged to monitor the health status of some industrial assets in real-time manner. To be specific, SHM involves a sensory system, a data acquisition system, a data management and interpretation system [2]. To satisfy SHM, the sensory system is permanently installed into the structures. An ideal sensor should be small in size and light in weight, and easily to be embedded into or surface-mounted onto the structure. In this regard, piezoelectric wafers and optic fibres are two types of transducers widely applied.

There are a variety of methods to develop SHM [3]. Of particular interest are guided-waves-based methods. Guided waves, acousto-ultrasonic waves confined inside a waveguide, have many advantages over longitudinal waves or transverse waves. As an elastic disturbance propagating omnidirectionally inside the structures, guided waves can interrogate a large area with only a few transducers. In terms of wave scattering effects such as reflection, refraction, attenuation and mode conversion due to the interaction of guided waves with structural damage, the location and severity of the possible damage can be determined. Moreover, working in a high frequency range, guided waves (with short wavelength in the order of hundred micrometers) are sensitive to microscopic damage in

the early stage of development, which is quite meaningful for high speed railway monitoring. Last but not the least, guided waves have the ability to test inaccessible or hidden components as well.

Nevertheless, a captured guided wave signal often appears complicated due to multiple wave modes, wave dispersion, boundary reflection and measurement noise, *etc.*, all of which result in difficulty in signal interpretation [3]. To tackle this problem, diagnostic imaging methods have been more and more preferred from the community. Diagnostic imaging attempts to describe the health status of the structure under inspection using an easily interpretable and intuitional image. The structure under inspection is meshed into many elements. Each element is endowed with a pixel value that corresponds to the probability of damage presence. Using such a greyscale image, the health status of the structures can be easily examined.

Intensive research activities have been directed to the field of diagnostic imaging [4-14]. As a representative, Tomography, a mature technology in medical imaging, has demonstrated effectiveness in damage identification. However, to reconstruct a tomogram requires extremely dense wave sensing paths, resulting in the consumption of a large number of transducers, therefore limiting its application for online monitoring. To circumvent such a deficiency, novel diagnostic imaging using limited number of sensors have been developed by taking advantage of sensor networks. Representatively, Ihn and Chang [5], Michaels *et al.* [7,8], Ostachowicz *et al.* [9,10] and Su *et al.* [3,4] developed various ToF-based diagnostic imaging to quantify the possible damage in the engineering structures. The damage-scattered wave packets (residual signal) are extracted by comparing a current signal with a baseline signal. It is noted that, to enhance the recognisability of the damage-scattered

wave signals, novel signal processing tools such as empirical mode decomposition (EMD), singular value decomposition (SVD), wavelet transform (WT) and Hilbert transform (HT) are often employed as auxiliary tools [15-17]. Different from ToF-based methods, Zhao *et al.* [11] introduced a correlation analysis-based technique for health monitoring of an aircraft wing. The correlation coefficient between the current and baseline signals is used as a key factor that indicates the health status of a structure under inspection. As another diagnostic imaging technique, phased-array has been preferred in recent years [12]. By steering the resulting wave beam (*i.e.* beamforming), the structure under inspection can be scanned in every direction. Moreover, Hoon *et al.* developed a novel imaging method to inspect hidden damage in a steel bridge [18-20]. It is a promising non-contact method since laser beams is used to excite and sense guided waves. In addition, Su *et al.* [21] developed a novel diagnostic imaging method to detect fatigue cracks. Nonlinear features of guided waves are extracted and fused, in consideration of strong nonlinearity presented by fatigue cracks.

As summarized above, current diagnostic imaging are mostly two-dimensional imaging methods, well suited for thin plate-like structures. For complex three-dimensional solid structures, it is still challenging due to the captured complicated guided wave signals caused by much more boundary reflection and multiple wave modes *etc.*. It is such a deficiency that has motivated the present work. In this study, by taking advantage of the signal features extracted from guided wave signals, a three-dimensional diagnostic imaging method was developed, able to depict the health status of complex solid structures. A part of a rail structure was prepared and subsequently cracked to simulate the real structural damage. With the assistance of an active sensor network in conformity to a pitch-catch configuration, the crack was clearly located. The FE simulation and experimental results have demonstrated the effectiveness of the developed three-dimensional imaging method.

## 2. Three-dimensional Diagnostic Imaging

To fulfil diagnostic imaging, a structure under inspection is first meshed into many nodes. Each node was subsequently endowed with a pixel value, termed *field value* in what follows. In such a way, a grey-scale image can be projected indicating the overall health status of the structure. The key point of diagnostic imaging is to establish the relationship between the *field value* of a certain spatial point and the probability of damage presence at that point, which is linked to the selected signal features from guided waves signals. In this study, the time-of-flight-based field value was applied.

### 2.1 Time-of-flight-based Field Value

ToF, *i.e.* time-of-flight, defined as the time consumed for a wave packet to propagate a certain distance, is one of the most straightforward features of a wave signal. Considering a sensor network consisting of $N$ PZT wafers, each wafer can serve as either an actuator or a sensor in terms of the dual piezoelectric effect, forming $N(N-1)$ actuator-sensor wave sensing paths. Without losing generality, focus on an arbitrary actuator-sensor wave sensing path, $A_i - S_j$ ($i, j = 1,\ 2,\ \cdots,\ N$, but $i \neq j$) in the Cartesian coordinate system ($A_i$ at the origin, $S_j$ at $(x_j, y_j, z_j)$ and the damage centre at $(x_D, y_D, z_D)$), as shown in Fig. 1. It should be noted that, different from the planar reference coordinate system used in traditional diagnostic imaging [4,5,7,9], the spatial reference coordinate system was adopted to satisfy the novel three-dimensional imaging. As indicated above, the guided waves in a complex solid structure are extremely complicated due to the multiple wave modes and boundary reflection. To circumvent such problems, the first-arrived-wave mode (abbreviated as *FAW* in what follows) of the guided waves was selected to monitor the structure under inspection. Provided that velocity $V$ of *FAW* mode is constant before and after interaction with damage, there exists a set of nonlinear equations for the sensor

network

$$(\frac{L_{A_i-D}}{V}+\frac{L_{D-S_j}}{V})-\frac{L_{A_i-S_j}}{V}=\Delta t_{i-j} \qquad (i, j=1,\ 2,\ \cdots,\ N \text{, but } i\neq j), \qquad \textbf{(1)}$$

where

$$L_{A_i-D}=\sqrt{x_D{}^2+y_D{}^2+z_D{}^2}\ , \quad L_{D-S_j}=\sqrt{(x_D-x_j)^2+(y_D-y_j)^2+(z_D-z_j)^2}\ ,$$

$$L_{A_i-S_j}=\sqrt{x_j{}^2+y_j{}^2+z_j{}^2}\ .$$

$\Delta t_{i-j}$ is the difference between (i) the ToF for the incident wave to travel from actuator $A_i$ to the damage and then to sensor $S_j$, and (ii) the ToF for the incident wave to travel directly from $A_i$ to $S_j$. $L_{A_i-D}$, $L_{D-S_j}$ and $L_{A_i-S_j}$ are the distances between $A_i$ and the damage, the damage and $S_j$, and $A_i$ and $S_j$, respectively. As we know, for a plate-like structure (without the consideration of the *z*-coordinate), Eq. (1) depicts a series of ellipse-like loci with $A_i$ and $S_j$ being two foci, indicating possible damage locations. However, for a complex solid structure, Eq. (1) depicts a series of complicated spatial curves, which are the prior perceptions with regard to the presence of damage, to be discussed in the following.

Further, the spatial structure under inspection is meshed using $K\times L\times M$ nodes virtually (each mesh node exclusively corresponds to a field value that indicates the possibility of damage presence there). It is assumed that the mesh nodes that right locate on the spatial curves perceived by Eq. (1) have the highest probability of damage presence; and for other mesh nodes, the greater the distance to the spatial curves, the lower the probability that damage exists there. To quantify the probabilities at all nodes, a *cumulative distribution function* (CDF), $F(c_{ij})$, is introduced, defined by,

$$F(c_{ij}) = \int_{-\infty}^{c_{ij}} f(c) \cdot dc, \quad \textbf{(2)}$$

where $f(c) = \frac{1}{\sigma_{ij}\sqrt{2\pi}} \exp[-\frac{c^2}{2\sigma_{ij}^2}]$ is the *Gaussian distribution function*, representing the probability density of damage presence at mesh node $(x_k, y_l, z_m)$, ( $k = 1, 2, \cdots, K; l = 1, 2, \cdots, L; m = 1, 2, \cdots, M$ ), established by actuator-sensor sensing path $A_i - S_j$. $c_{ij} = \left\| \chi_i - \mu_{ij} \right\|$, where $\chi_i$ is the location vector of node $(x_k, y_l, z_m)$ and $\mu_{ij}$ is the location vector of the point on the spatial curves perceived by Eq. (1) that has the shortest distance to $(x_k, y_l, z_m)$. $\sigma_{ij}$ is the standard variance. Given a distance, $c_{ij}$, the probability of damage presence at $(x_k, y_l, z_m)$, $I(x_k, y_l, z_m)$, established by $A_i - S_j$, is defined as

$$I(x_k, y_l, z_m) = 1 - \left[ F(c_{ij}) - F(-c_{ij}) \right]. \quad \textbf{(3)}$$

Upon Eq. (3), *field value* of every node of the spatial structure under inspection could be calculated, by taking advantage of the extracted ToF-based signal features.

### 2.2 Image Fusion

For every single actuator-sensor wave sensing path (*i.e.* $A_i - S_j$, $i, j = 1, 2, \cdots, N$, but $i \neq j$) rendered by the sensor network, the prior probability of the damage presence was quantified at every position of the structure under inspection in terms of Eq. (3), resulting in a source image indicating the health status of the structure. Source images contain, however, not only the desired damage-scattered waves, but also unwanted features including various noise, multiple wave modes and multiple wave reflection from boundaries *etc.*. To reduce imprecision and uncertainties, and simultaneously retain the

useful information from the source images, an image fusion technique was required to create a synthetic and improved image.

Image fusion, *i.e.* pixel-level fusion, which determines the pixel value of the fused image from those of source images, has been widely applied in many fields [3]. For example, Infra-red and visible images may be fused as an aid to pilots landing in poor weather, or Computed Tomography (CT) images may be fused as an aid to medical diagnosis. Perhaps the most direct approach to fusion is to sum and average the source images. However when the direct method is applied, the contrast of features may be reduced. Therefore, many studies have focused on a wavelet-based fusion which holds the capability of selecting desirable features [22]. In this technique, the composite image is constructed not a pixel at a time, but a feature at a time. Salient features are identified in every source image, and then are copied to the composite image. While less salient features that may partially mask the more salient features are discarded. For damage identification, image fusion can be seen a route from individual prior perceptions to ultimate posterior consensus.

In this study, two types of image fusion schemes were applied and compared. Considering a sensor network consisting of $N$ PZT wafers, $N(N-1)$ actuator-sensor wave sensing paths can be formed in terms of the dual piezoelectric effect. Every single actuator-sensor wave sensing path exclusively creates one source image, described by $P(E|S_j)$, where the subscript $j$ represents the $j^{th}$ sensing path. Consequently, the entire sensor network contributes $N(N-1)$ source images in total, which are subsequently fused by the following equations,

*arithmetic* mean scheme:
$$P_{arithmetic} = \frac{1}{N(N-1)} \sum_{j=1}^{N(N-1)} P(E|S_j), \quad \textbf{(4)}$$

*geometric* mean scheme: $$P_{geometric} = \left( \prod_{j=1}^{N(N-1)} P(E|S_j) \right)^{\frac{1}{N(N-1)}}. \quad \textbf{(5)}$$

## 3. FE Simulation

To examine the feasibility of the developed three-dimensional diagnostic imaging technique, a part of a rail structure was considered, with the geometrical properties shown in Fig. 2. Nine circular PZT wafers (diameter: 10 mm, thickness: 1 mm), denoted by $T_i$ ($i = 1,\ 2,\ \cdots,\ 9$), were allocated onto the structure. To better the description, a A-A sectional view was displayed in Fig. 2(b), showing $T_i$ ($i = 1,\ 2,\ \cdots,\ 6$) allocated on the lower surface. A crack with a dimension of 20 mm long, 1 mm wide and 1.5 mm deep, was assumed in the structure, as shown in Fig. 2(a).

The rail model was meshed using three-dimensional eight-node brick elements, as shown in Fig. 3(a). The crack was formed by removing associated FE elements from the rail model, as displayed in Fig. 3(b). A three-cycle Hanning-window-modulated sinusoid tone bursts at a central frequency of 200 kHz was applied as the input excitation signal. To generate guided waves, in-plane displacement constraints was imposed onto the nodes along the radial direction of the simulated PZT actuator, as exhibited in Fig. 3(c). Dynamic simulation was implemented using ABAQUS®/EXPLICIT. To ensure the precision, the largest dimension of the elements was set to be 1 mm, guaranteeing at least ten elements were allocated per wavelength. The calculation time of each step was controlled to be less than the ratio of the distance of any two adjacent FE nodes to the maximum velocity of the selected guided wave mode.

## 4. Experimental Setup

To demonstrate the effectiveness of the developed three-dimensional diagnostic imaging technique, a part of a rail structure was prepared, as photographed in Fig. 4, with the same geometrical properties and configurations used in FE simulation. The part of rail was first carefully polished to reach a substantial coupling between the transducers and the host structure. Nine circular PZT wafers (diameter: 10 mm, thickness: 1 mm) were subsequently surface-mounted onto the structure. A thin layer of two-component conductive adhesive was applied, making the transducers be grounded and eliminating the need for additional electrodes. A lead wire was soldered onto the top surface of each PZT wafer to serve as signal wire. Shielded wires and standard BNC connectors were used to minimize measurement noise.

The signal generation and acquisition system used in this study consists of three units, *i.e.* an arbitrary waveform generator (SDG5162), a linear power amplifier (PiezoSys® EPA-104) and an oscilloscope (SDS1204CFL). To be specific, a three-cycle Hanning-window-modulated sinusoid tone bursts at a central frequency of 200 kHz serving as an input excitation signal, was generated by the arbitrary waveform generator (SDG5162) and amplified using the linear power amplifier (PiezoSys® EPA-104) to 160 $V_{p\text{-}p}$. The amplified analog signal was subsequently applied to each PZT wafer, *i.e.* $T_i$ ($i = 1,\ 2,\ \cdots,\ 9$), in turn to generate diagnostic ultrasonic waves. Upon interaction with the structure under inspection, the guided waves signals were captured with the oscilloscope (SDS1204CFL) at a sampling rate of 25 MHz.

The procedure of the experiment is as follows: 1) the intact specimen was instrumented with the signal generation and acquisition system introduced as above to capture the

benchmark signals. 2) a crack with a dimension of 20 mm long, 1 mm wide and 1.5 mm deep, was introduced into the specimen using a saw, with its location and orientation shown in Fig. 2(a). 3) the current specimen with the crack was instrumented with the signal generation and acquisition system to capture the damaged signals. Upon the comparison of the signals captured in current status with those captured in intact status, the damaged-scattered-wave signals could be obtained and applied to develop the three-dimensional diagnostic imaging.

## 5. Results and Discussion

As mentioned above, a guided waves signal is extremely complicated due to multiple wave modes and boundary reflections. To circumvent such deficiency, the *FAW* mode (first-arrived-wave mode) of the guided waves was selected for damage detection. To accurately locate the damage, the velocity of *FAW* mode was determined at first. As a representative example, the guided waves signal captured via actuator-sensor wave sensing path $T_3 - T_6$ for the intact specimen from FE simulation was first displayed in Fig. 5(a). The input excitation signal was included in the same figure for a better comparison, *i.e.* a three-cycle Hanning-window-modulated sinusoid tone bursts at a central frequency of 200 kHz. The wave signals (both the input excitation signal and the benchmark signal) were normalized relative to their maximum magnitude, and subsequently processed with HT (Hilbert transform) to highlight energy concentration, as shown in Fig. 5(b). Upon HT, the ToF of the incident *FAW* mode was determined by the time interval between the two peaks of the two HT-processed envelopes, as shown in Fig. 5(b). With the distance between $T_3$ and $T_6$ measured to be 206 mm, the ToF measured to be 44.44 $\mu s$, the velocity of the *FAW* mode was calculated to be 4635 $m/s$. To make a comparison, the guided waves signal captured

via actuator-sensor wave sensing path $T_3 - T_6$ for the intact specimen from experiment was displayed in Fig. 6. Repeated the procedure mentioned above, the velocity of the *FAW* mode was measured to be 4720 $m/s$ in experiment. The experiment and FE simulation match well with each other, with a relative difference less than 2%.

To determine the ToF of the damage-scattered *FAW* mode, both the current (damaged) and corresponding baseline signals (benchmark) provided by actuator-sensor wave sensing path $T_3 - T_6$ from experiment were exhibited in Fig. 7(a), normalized relative to the maximum magnitude of the baseline signal. The residual signal was subsequently acquired by subtracting the baseline signal from the current signal, as shown in Fig. 7(b), from which the damage-scattered wave packet were clearly seen. Similar as above, the residual signal was then treated with HT-based signal processing, so as to depict the wave energy distribution, as displayed in Fig. 7(c). Upon HT, the ToF of the damage-scattered *FAW* mode was measured to be 58.08 $\mu s$ .

With the ToF extracted from the captured guided waves signals, *field value* of every node of the rail structure perceived by a certain actuator-sensor wave sensing path can be calculated via Eqs. (1), (2) and (3), resulting in a source image indicating the health status of the structure. As a typical example, the source image established by sensing path $T_3 - T_6$ was displayed in Fig. 8. Different from the two-dimensional source images established in traditional diagnostic imaging, three-dimensional source images were constructed in line with the geometrical properties of the structure, *i.e.* a rail-like source image in this study. In the source image, the light zones (with a large field value) implies a high probability of damage presence there, whereas, the dark zones means healthy (with a small field value). As is shown in Fig. 8, the lightest zones (with the largest field value) constitutes a

complicated spatial curves instead of ellipse-like root loci in two-dimensional diagnostic imaging.

The source images perceived by actuator-sensor wave sensing paths $T_3 - T_8$ and $T_2 - T_4$ were exhibited in Figs. 9(a) and (b), respectively, for a comparison. It can be seen that different patterns of source images are obtained *via* different wave sensing paths. The source images look like a series of spatial curves, indicating the possible damage locations. This results from the crucial equation that is used to develop field value, *i.e.* Eq. (1), which is established in three-dimensional space, instead of ellipse-like planar source images controlled in two-dimensional plane. It should be pointed out that, the three-dimensional source images contain much noise and various uncertainties, making damage identification much difficult.

Repeating the above procedures, source images contributed by $9 \times 8 = 72$ actuator-sensor wave sensing paths provided by the sensor network were established, and then fused using the developed image fusion schemes. The ultimate fused images using arithmetic mean scheme (Eq. (4)) and geometric mean scheme (Eq. (5)) were exhibited in Figs. 10(a) and (b), respectively. From the images, the crack is successfully located, showing the effectiveness of the developed three-dimensional diagnostic imaging. It can be clearly seen that, the damage is more easily identified in Fig. 10(b) instead of Fig. 10(a). This is due to the fact that, the arithmetic mean equally balances all source images, making salient features (damage-related features) become de-emphasized in the ultimate fused image and meanwhile noise and uncertainties stand out. In contrast, geometric mean possesses capability of de-noising since it highlights salient features in common.

To further examine the effectiveness of the developed diagnostic imaging technique, several PZT wafers were abandoned to form more specimen configurations. The ultimate resulting images upon arithmetic mean fusion scheme using nine PZT wafers (*i.e.*, $T_i$, $i = 1,\ 2,\ \cdots,\ 9$), seven PZT wafers (*i.e.*, $T_i$, $i = 2,\ 3,\ \cdots,\ 8$) and five PZT wafers (*i.e.*, $T_i$, $i = 3,\ 4,\ \cdots,\ 7$) were exhibited in Fig. 11(a), (b) and (c), respectively. With the reduction of the number of PZT wafers, the identification accuracy decreases as well. It was clearly seen that pseudo damage stand out with very high value of probability of damage presence as sensor number decreases. To make a comparison, the ultimate resulting images upon geometric mean fusion using the same specimen configurations were exhibited in Fig. 12. It was observed that the fused results using geometric mean were better than those using arithmetic mean since much noise was removed. But as envisaged, there still exist pseudo damage with extremely high value of probability of damage presence, masking the real damage location, as was shown in Fig. 12(c).

As mentioned above, a surface crack was successfully located using the developed three-dimensional diagnostic imaging approach. In practice, many engineering structures are prone to interior or hidden damage, difficult to be examined. To address this concern, FE simulation was conducted to inspect a hidden crack inside the rail specimen. The location of the crack was exhibited in Fig. 13(a), with a dimension of 20 mm long, 1 mm wide and 2 mm deep. The ultimate fused images using arithmetic mean scheme and geometric mean scheme were exhibited in Figs. 14(a) and (b), respectively. It was clearly seen that the interior crack was successfully located. This is due to the fact that, guided waves have the capacity to test the interior of a structure, different from surface waves. Moreover, the developed diagnostic imaging approach is a three-dimensional method, capable of imaging the interior of a structure.

It should be noted that, although the damage can be successfully located (Fig. 10(b) and 14(b)), the identification accuracy remains to be improved. This is due to the approximation applied when developing the field values. As a typical example shown in Fig. 15, an actuator-sensor wave sensing path $T_2 - T_7$ is taken into account. In the imaging method, the linear path is considered, *i.e.* the dash dot line connecting $T_2$ with $T_7$. However, the ultrasonic waves are guided by the rail structures, therefore following a curved path, *i.e.* the solid line connecting $T_2$ with $T_7$. It is such approximation that reduce the identification accuracy. On the other hand, the image fusion schemes applied in this study have yet to be improved. More sophisticated image fusion methods capable of selecting desirable features, discarding unwanted noise and uncertainties, will be considered in future studies.

## 6. Conclusion

Different from plate-like structures, inspection of complex solid structures is more problematic, attracting intensive research strength. Ultrasonic waves guided in solid structures are extremely complicated due to various wave modes, multiple boundary reflections and wave dispersion phenomenon, *etc.*. In this study, a three-dimensional diagnostic imaging technique was developed to circumvent such problems. ToF-based signal features were extracted from captured guided waves signals with the assistance of an active sensor network, which were then applied to develop field values of source images. Upon the developed image fusion schemes, the source images perceived by every actuator-sensor wave sensing paths were fused. The ultimate fused images have shown satisfactory results in detecting a crack introduced into a part of rail structure.

**Acknowledgement**

The work was supported by Foundation for Distinguished Young Talents in Higher Education of Guangdong (2013LYM_0068), National Natural Science Foundation of China (51375414, 51275099, 51305086, 51205072, 51575115 and 61403089), the Hong Kong Research Grants Council via General Research Funds (523313), and chief scientist of Guangzhou Yangcheng Scholars (12A006S).

**References**

[1] S. Y. Chong, J.-R. Lee, and H.-J. Shin, "A review of health and operation monitoring technologies for trains," *Smart Structures and Systems,* vol. 6, pp. 1079-1105, 2010.

[2] K.-y. Wong, C. K. Lau, and A. R. Flint, "Planning and implementation of the structural health monitoring system for cable-supported bridges in Hong Kong," in *Nondestructive Evaluation of Highways, Utilities, and Pipelines IV*, Newport Beach, CA, USA, 2000, pp. 266-275.

[3] Z. Q. Su and L. Ye, *Identification of Damage Using Lamb Waves: From Fundamentals to Applications*. London: Springer-Verlag GmbH & Co., 2009.

[4] Z. Q. Su, X. M. Wang, L. Cheng, L. Yu, and Z. P. Chen, "On selection of data fusion schemes for structural damage evaluation," *Structural Health Monitoring: An International Journal,* vol. 8, pp. 223-241, 2009.

[5] J.-B. Ihn and F.-K. Chang, "Pitch-catch active sensing methods in structural health monitoring for aircraft structures," *Structural Health Monitoring: An International Journal,* vol. 7, pp. 5-19, 2008.

[6] K. Lonkar and F.-K. Chang, "Modeling of piezo-induced ultrasonic wave propagation in composite structures using layered solid spectral element," *Structural Health Monitoring: An International Journal,* vol. 13, pp. 50-67, 2014.

[7] J. E. Michaels, "Detection, localization and characterization of damage in plates with an in situ array of spatially distributed ultrasonic sensors," *Smart Materials and Structures,* vol. 17, 2008.

[8] J. S. Hall and J. E. Michaels, "Multipath ultrasonic guided wave imaging in complex structures," *Structural Health Monitoring: An International Journal,* vol. 14, pp. 345-358, 2015.

[9] W. M. Ostachowicz, P. Kudela, P. Malinowski, and T. Wandowski, "Damage localisation in plate-like structures based on PZT sensors," *Mechanical Systems and Signal Processing,* vol. 23, pp. 1805-1829, 2009.

[10] T. Wandowski, P. Malinowski, and W. M. Ostachowicz, "Circular sensing networks for guided waves based structural health monitoring," *Mechanical Systems and Signal Processing,* vol. 66, pp. 248-267, 2015.

[11] X. Zhao, H. Gao, G. Zhang, B. Ayhan, F. Yan, C. Kwan, and J. L. Rose, "Active health monitoring of an aircraft wing with embedded piezoelectric sensor/actuator

network: I. Defect detection, localization and growth monitoring," *Smart Materials and Structures,* vol. 16, pp. 1208-1217, 2007.
[12] G. Victor, R. Catalin, L. Bin, and F. Erik, "Omnidirectional piezo-optical ring sensor for enhanced guided wave structural health monitoring," *Smart Materials and Structures,* vol. 24, 2015.
[13] F. Yan, R. L. Royer, and J. L. Rose, "Ultrasonic guided wave imaging techniques in structural health monitoring," *Journal of Intelligent Material Systems and Structures,* vol. 21, pp. 377-384, 2010.
[14] Y. Wang, L. Gao, S. Yuan, L. Qiu, and X. Qing, "An adaptive filter-based temperature compensation technique for structural health monitoring," *Journal of Intelligent Material Systems and Structures,* vol. 25, pp. 2187-2198, 2014.
[15] A. Bagheri, K. Li, and P. Rizzo, "Reference-free damage detection by means of wavelet transform and empirical mode decomposition applied to Lamb waves," *Journal of Intelligent Material Systems and Structures,* vol. 24, pp. 194-208, 2013.
[16] L. Lei, L. Shuntao, and Y. Fuh-Gwo, "Damage localization using a power-efficient distributed on-board signal processing algorithm in a wireless sensor network," *Smart Materials and Structures,* vol. 21, 2012.
[17] S. K. Yadav, S. Banerjee, and T. Kundu, "On sequencing the feature extraction techniques for online damage characterization," *Journal of Intelligent Material Systems and Structures,* vol. 24, pp. 473-483, 2013.
[18] A. Yun-Kyu, S. Homin, and S. Hoon, "Wireless ultrasonic wavefield imaging via laser for hidden damage detection inside a steel box girder bridge," *Smart Materials and Structures,* vol. 23, 2014.
[19] A. Yun-Kyu, P. Byeongjin, and S. Hoon, "Complete noncontact laser ultrasonic imaging for automated crack visualization in a plate," *Smart Materials and Structures,* vol. 22, 2013.
[20] L. Peipei, S. Hoon, and P. Byeongjin, "Baseline-free damage visualization using noncontact laser nonlinear ultrasonics and state space geometrical changes," *Smart Materials and Structures,* vol. 24, 2015.
[21] Z. Q. Su, C. Zhou, M. Hong, L. Cheng, Q. Wang and X. Qing, "Acousto-ultrasonics-based fatigue damage characterization: linear *versus* nonlinear signal features," *Mechanical Systems and Signal Processing,* vol. 45, pp. 225-239, 2014.
[22] W. Xianghai, S. Yutong, Z. Zhiguang, and F. Lingling, "An image fusion algorithm based on lifting wavelet transform," *Journal of Optics*, vol. 17, 2015.

**Figure Captions**

**Figure 1** Relative positions among actuator $A_i$, sensor $S_j$ and damage in the local coordinate system for wave sensing path $A_i - S_j$

**Figure 2** The configurations of the rail specimen in (a) profile view; and (b) A-A sectional view

**Figure 3** (a) the FE model of a part of rail; (b) the crack model; and (c) the PZT actuator model

**Figure 4** The rail specimen containing a crack and nine PZT wafers

**Figure 5** (a) the input excitation signal and the baseline signal acquired via wave sensing path $T_3 - T_6$ from FE simulation; and (b) envelopes of energy distribution of signals in (a) obtained using HT;

**Figure 6** (a) the input excitation signal and the baseline signal acquired via wave sensing path $T_3 - T_6$ from experiment; and (b) envelopes of energy distribution of signals in (a) obtained using HT;

**Figure 7** (a) the current signal (damaged) and the baseline signal (benchmark) acquired via wave sensing path $T_3 - T_6$; (b) the input excitation signal and the residual signal acquired via wave sensing path $T_3 - T_6$ (the difference between the two signals in (a)); and (c) envelopes of energy distribution of signals in (b) obtained using HT

**Figure 8** The source image established by wave sensing path $T_3 - T_6$

**Figure 9** The source images established by wave sensing path (a) $T_3 - T_8$; and (b) $T_2 - T_4$

**Figure 10** Ultimate resulting images using (a) arithmetic mean fusion scheme; and (b) geometric mean fusion scheme (short solid line: real crack)

**Figure 11** Ultimate resulting images upon arithmetic mean fusion scheme using (a) nine PZT wafers (*i.e.*, $T_i$, $i = 1,\ 2,\ \cdots,\ 9$); (b) seven PZT wafers (*i.e.*, $T_i$,

$i = 2,\ 3,\ \cdots,\ 8$); and (c) five PZT wafers (*i.e.*, $T_i$, $i = 3,\ 4,\ \cdots,\ 7$)

**Figure 12** Ultimate resulting images upon geometric mean fusion scheme using (a) nine PZT wafers (*i.e.*, $T_i$, $i = 1,\ 2,\ \cdots,\ 9$); (b) seven PZT wafers (*i.e.*, $T_i$, $i = 2,\ 3,\ \cdots,\ 8$); and (c) five PZT wafers (*i.e.*, $T_i$, $i = 3,\ 4,\ \cdots,\ 7$)

**Figure 13** The specimen configurations to inspect an interior crack in (a) profile view; and (b) A-A sectional view

**Figure 14** Ultimate resulting images using (a) arithmetic mean fusion scheme; and (b) geometric mean fusion scheme (short dash line: real crack)

**Figure 15** Schematic of actuator-sensor wave sensing path $T_2 - T_7$ (solid line: real wave propagating path; dash dot line: assumed wave propagating path)

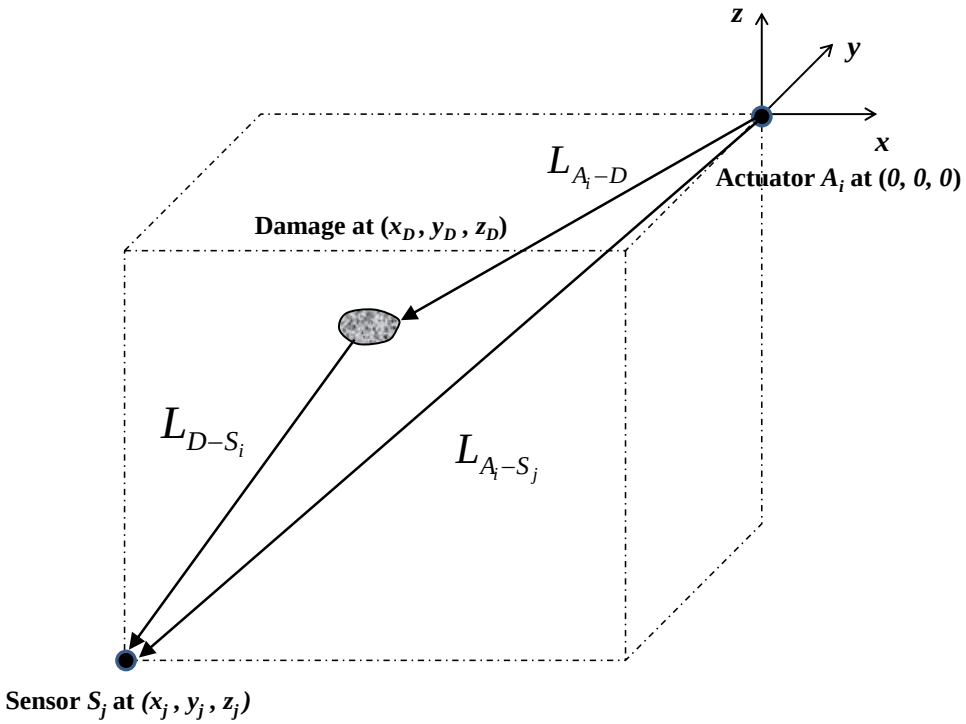
z
y
x
$L_{A_i-D}$
Actuator $A_i$ at (0, 0, 0)
Damage at ($x_D$, $y_D$, $z_D$)
$L_{D-S_i}$
$L_{A_i-S_j}$
Sensor $S_j$ at ($x_j$, $y_j$, $z_j$)

**Figure 1**

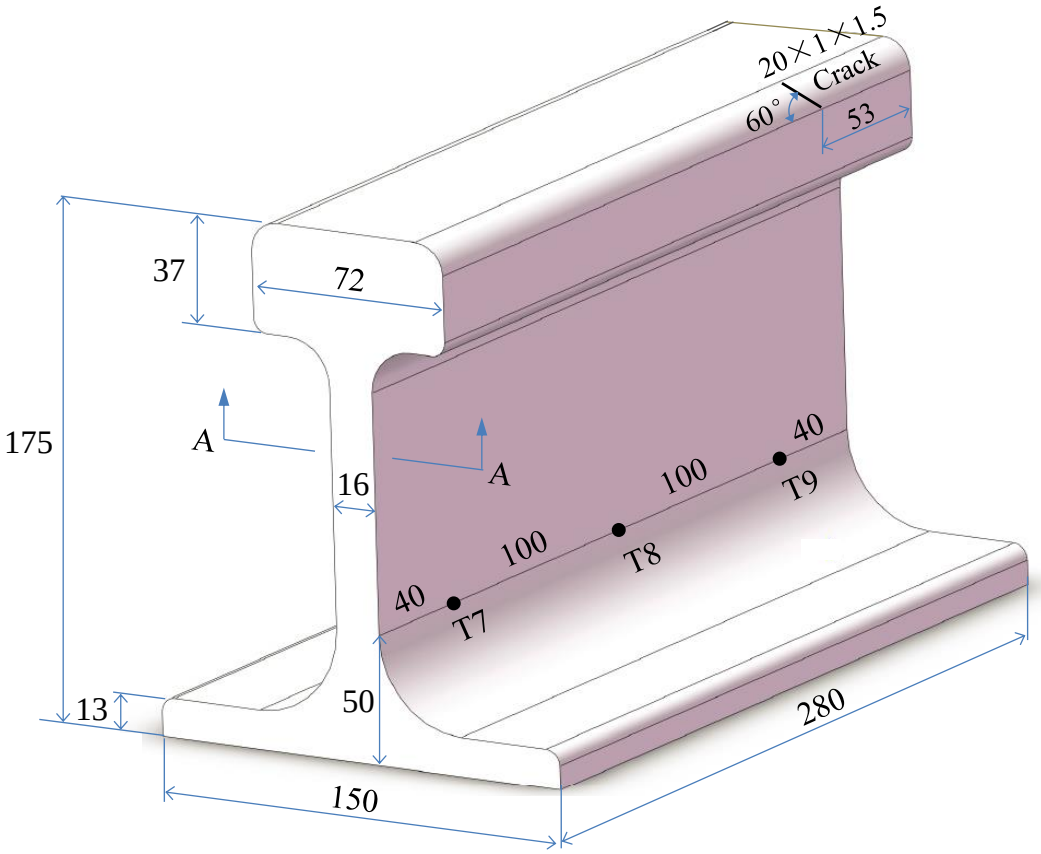


(a)

A—A

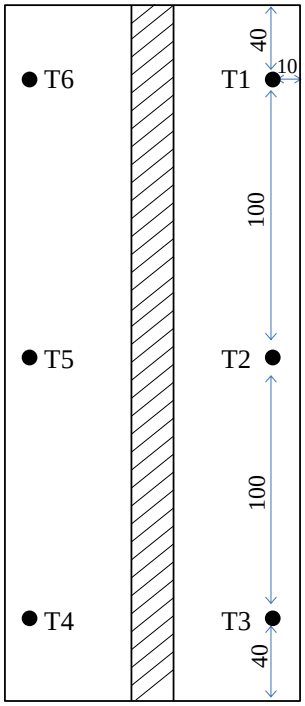


(b)

**Figure 2**

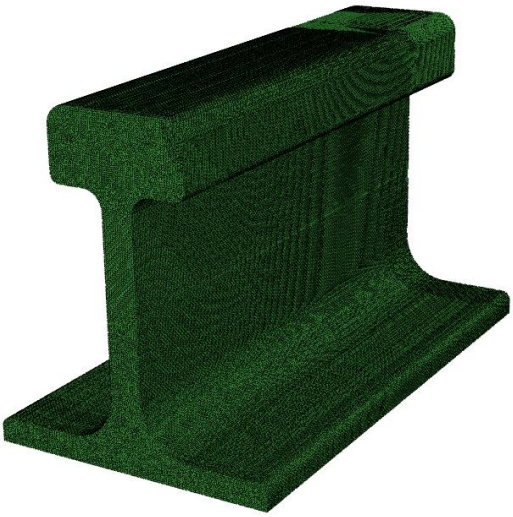

(a)

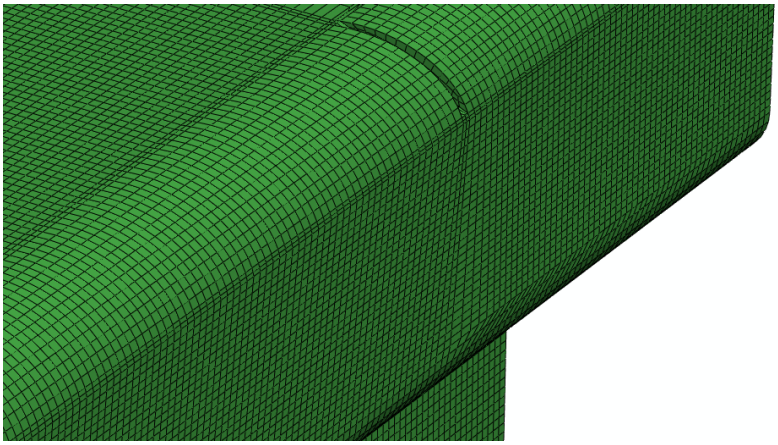

(b)

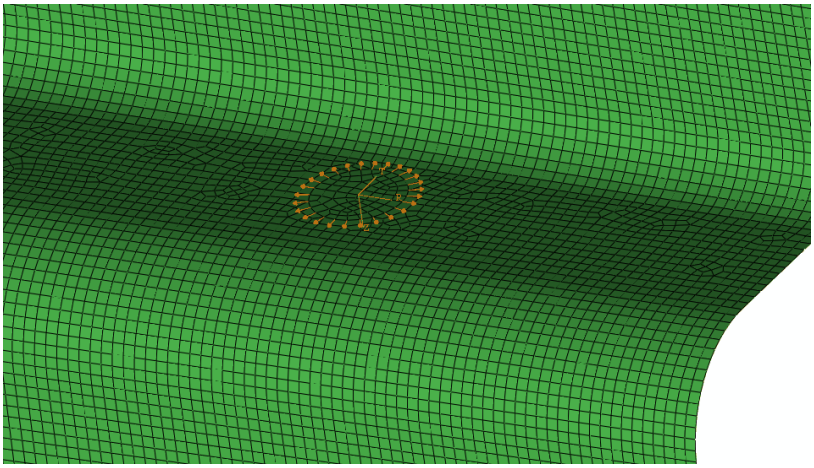

(c)

**Figure 3**

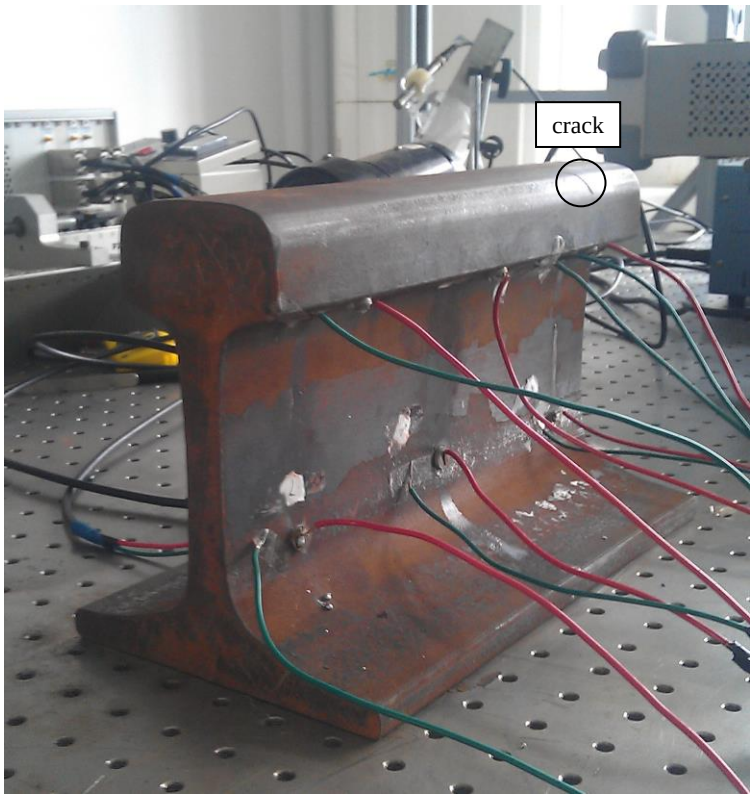


**Figure 4**

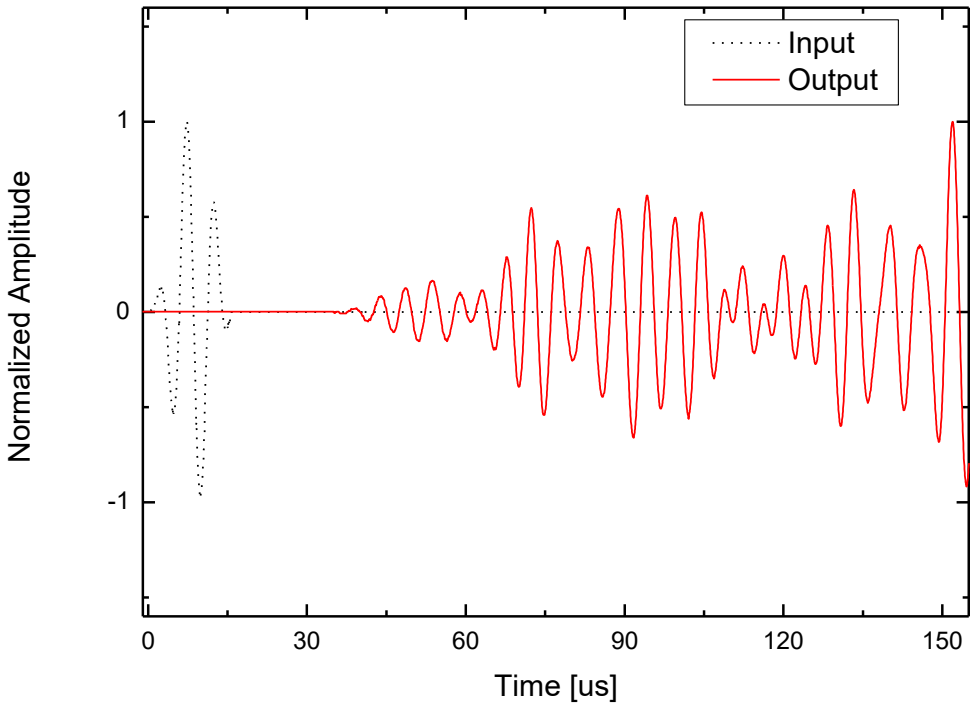
Input
Output
Normalized Amplitude
1
0
-1
0
30
60
90
120
150
Time [us]

(a)

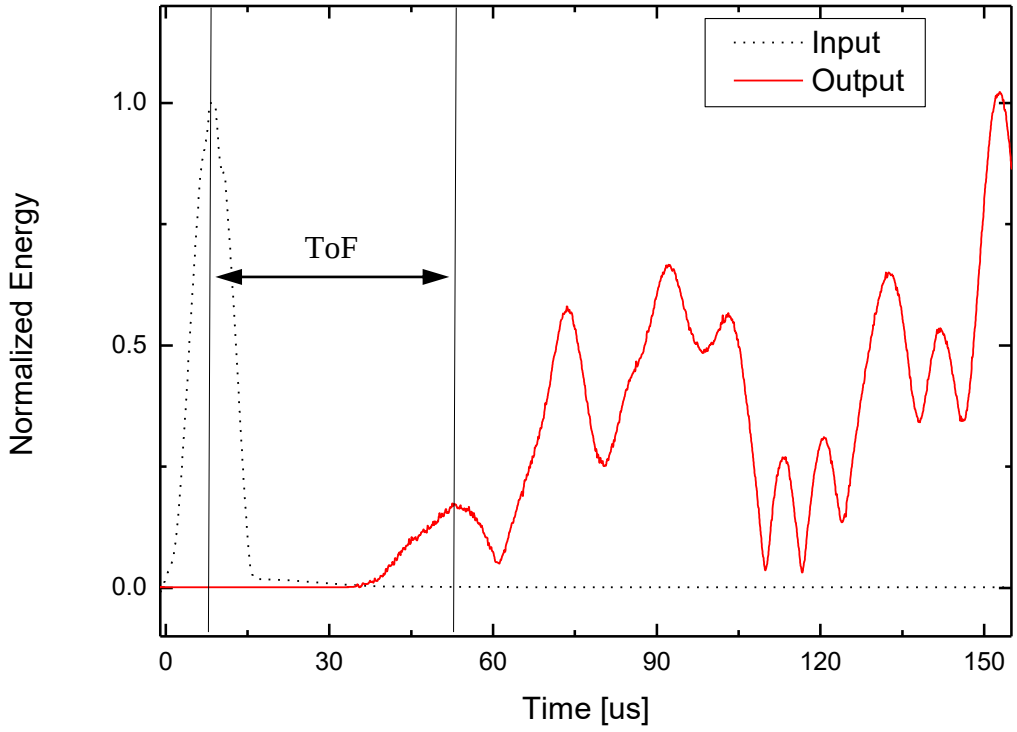
Input
Output
ToF
Normalized Energy
1.0
0.5
0.0
0
30
60
90
120
150
Time [us]

(b)

**Figure 5**

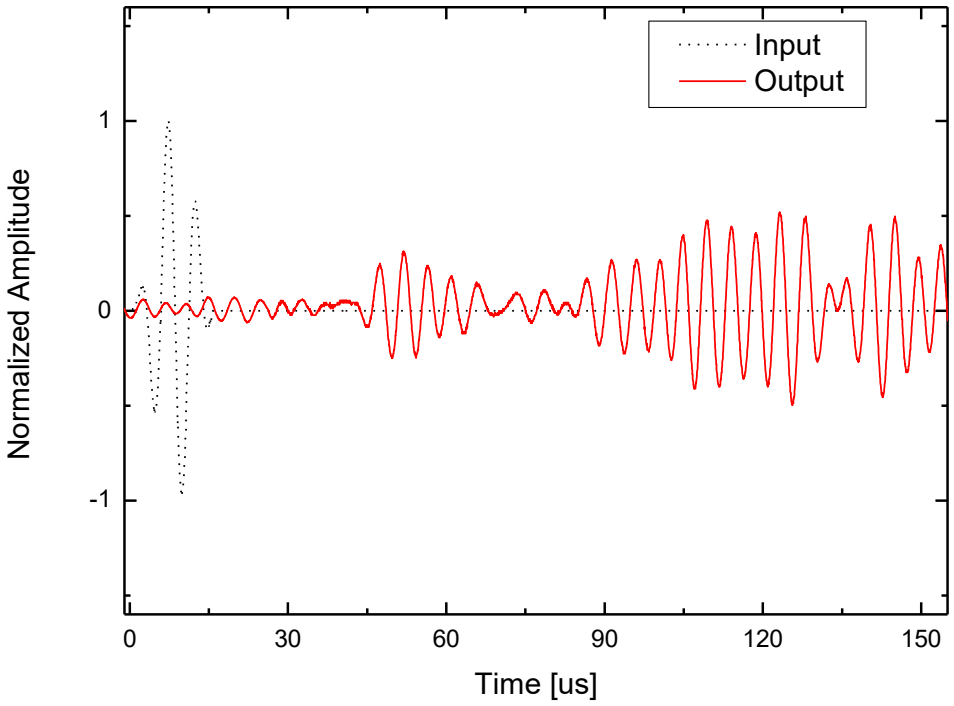
Input
Output
Normalized Amplitude
1
0
-1
0
30
60
90
120
150
Time [us]

(a)

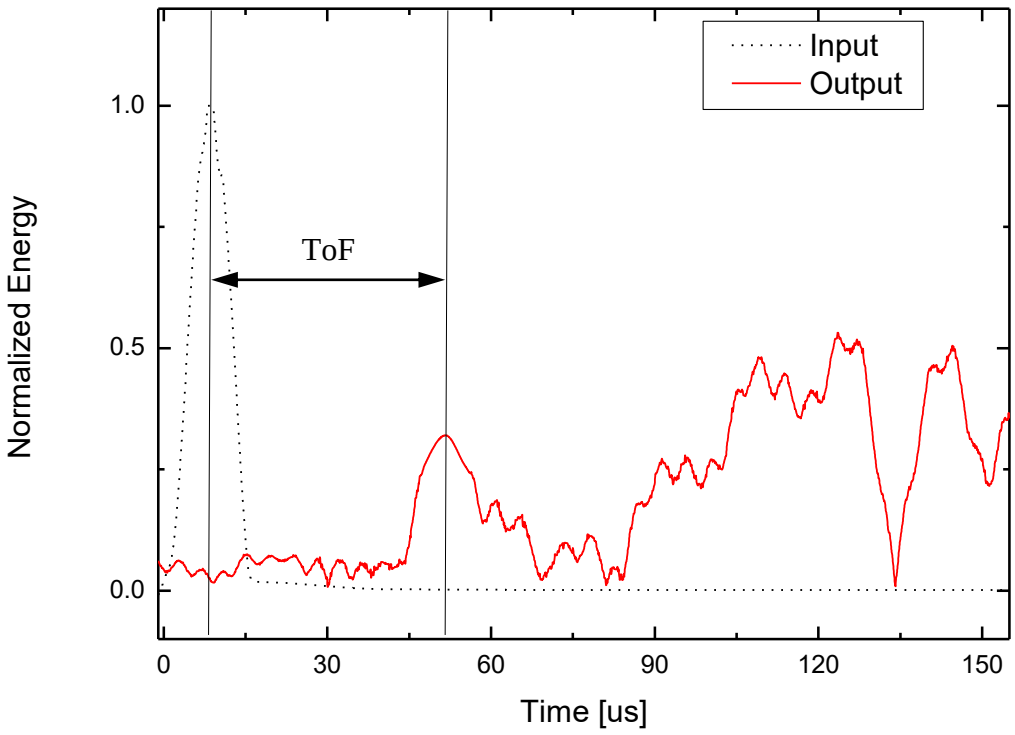
Input
Output
ToF
Normalized Energy
1.0
0.5
0.0
0
30
60
90
120
150
Time [us]

(b)

**Figure 6**

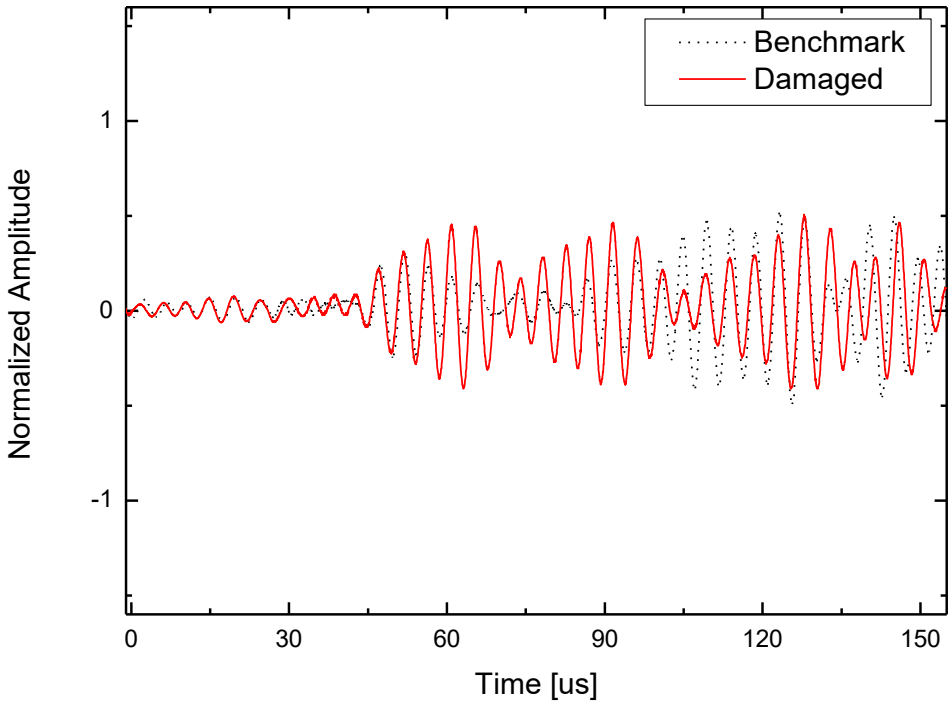
Benchmark
Damaged
Normalized Amplitude
1
0
-1
0
30
60
90
120
150
Time [us]

(a)

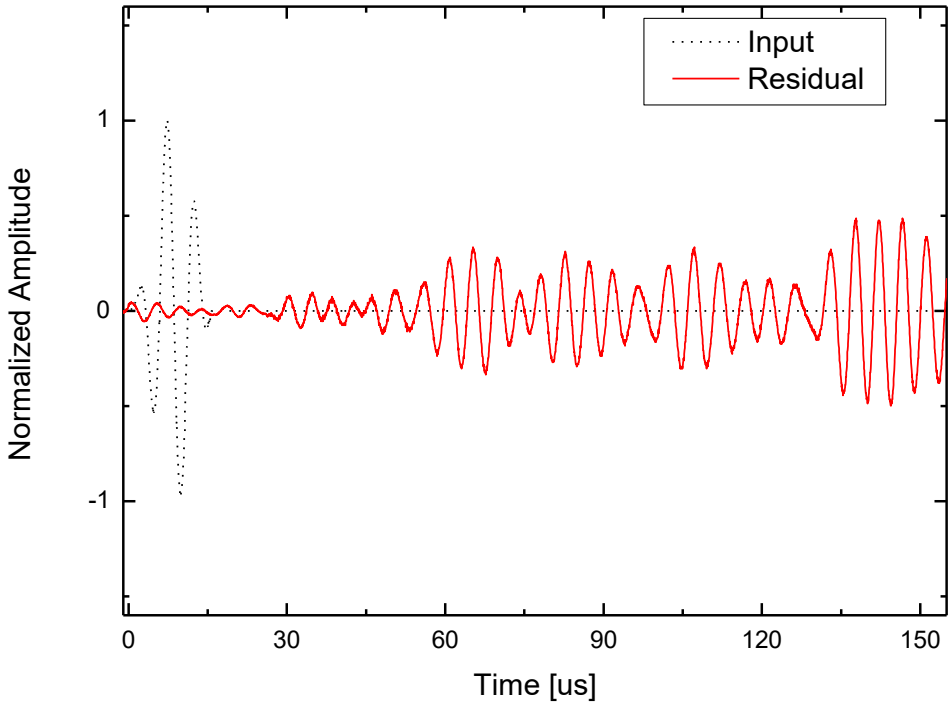
Input
Residual
Normalized Amplitude
1
0
-1
0
30
60
90
120
150
Time [us]

(b)

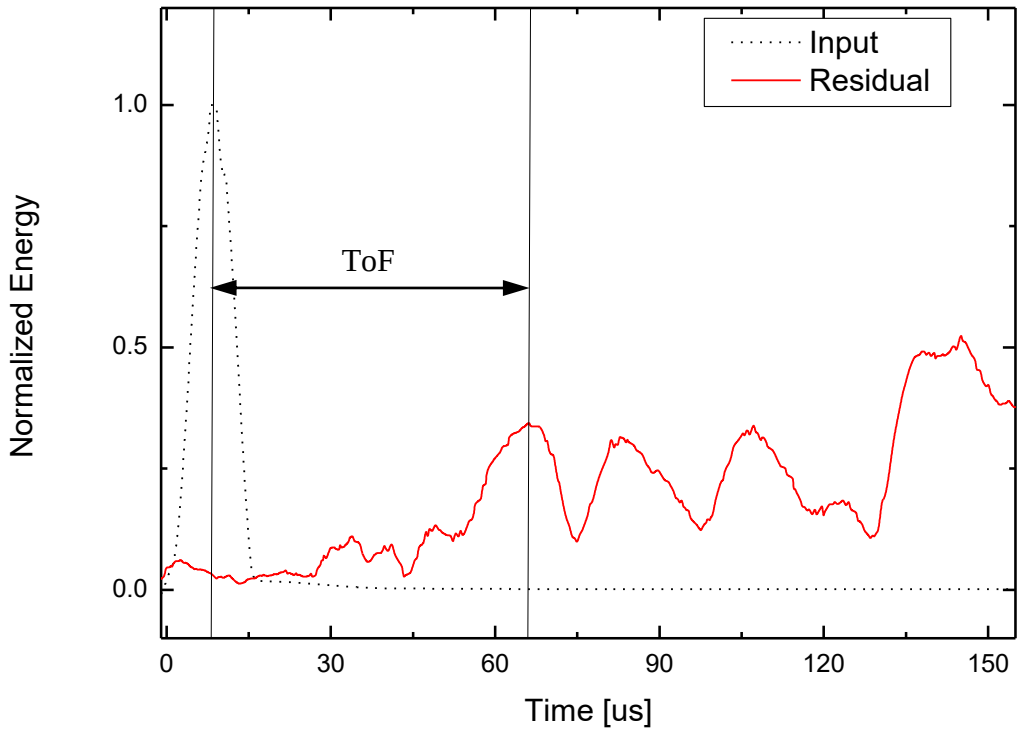
Input
Residual
ToF
Normalized Energy
1.0
0.5
0.0
0
30
60
90
120
150
Time [us]

(c)

**Figure 7**

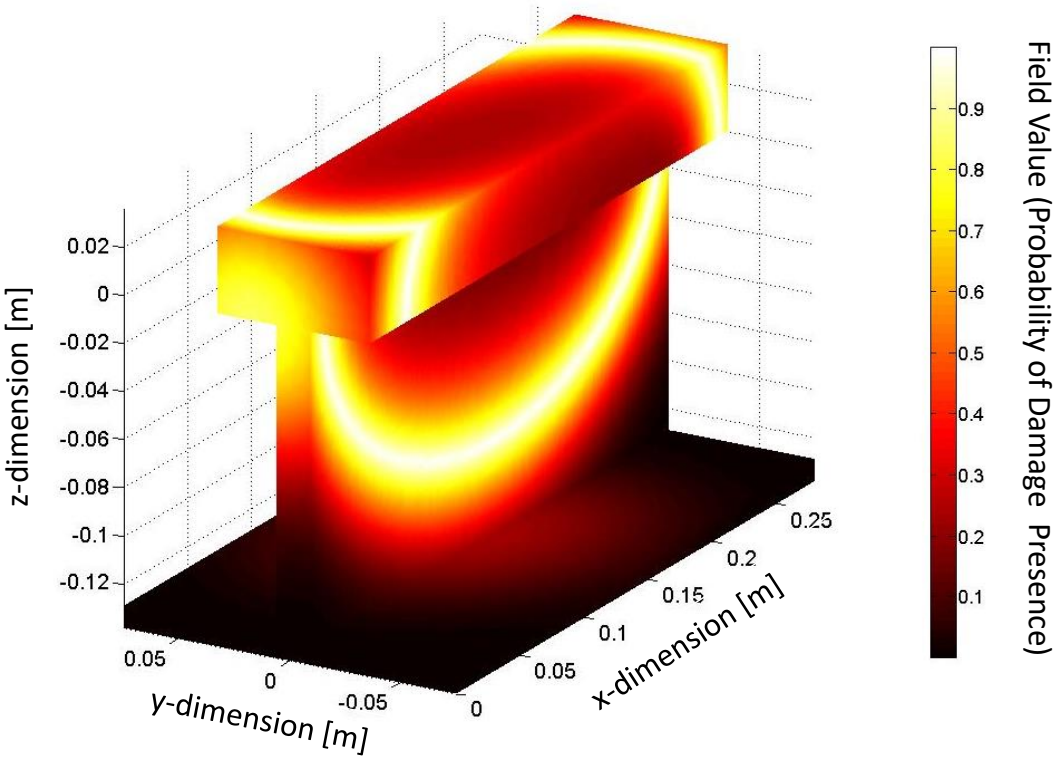
z-dimension [m]
0.02
0
-0.02
-0.04
-0.06
-0.08
-0.1
-0.12
0.05
0
-0.05
y-dimension [m]
0
0.05
0.1
0.15
0.2
0.25
x-dimension [m]
Field Value (Probability of Damage Presence)
0.9
0.8
0.7
0.6
0.5
0.4
0.3
0.2
0.1

**Figure 8**

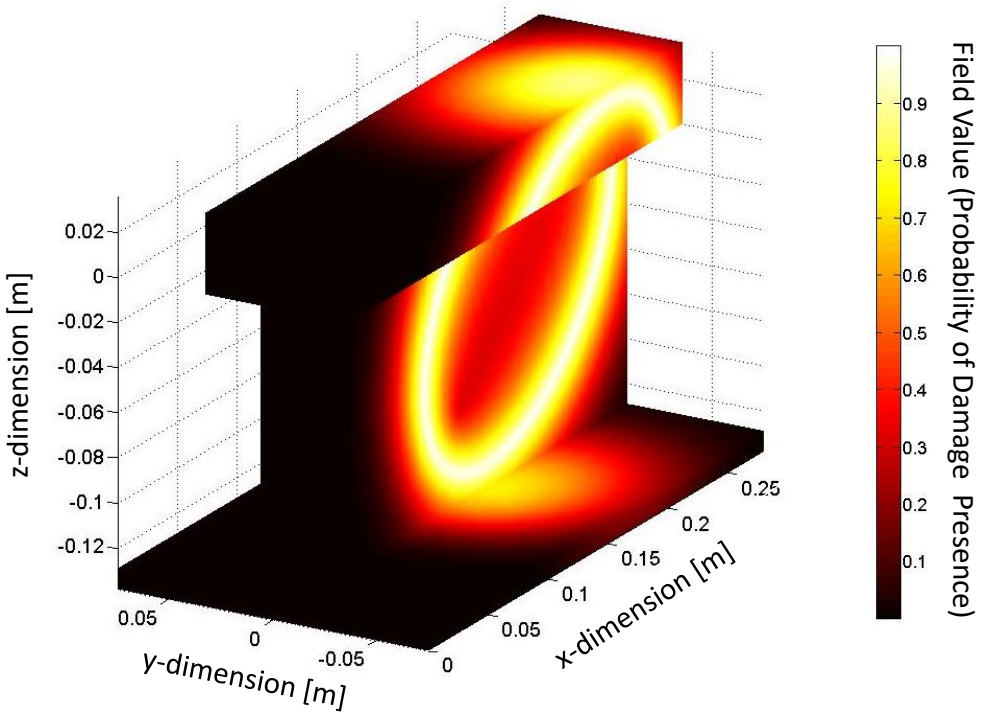
z-dimension [m]
0.02
0
-0.02
-0.04
-0.06
-0.08
-0.1
-0.12
y-dimension [m]
0.05
0
-0.05
x-dimension [m]
0
0.05
0.1
0.15
0.2
0.25
Field Value (Probability of Damage Presence)
0.9
0.8
0.7
0.6
0.5
0.4
0.3
0.2
0.1

(a)

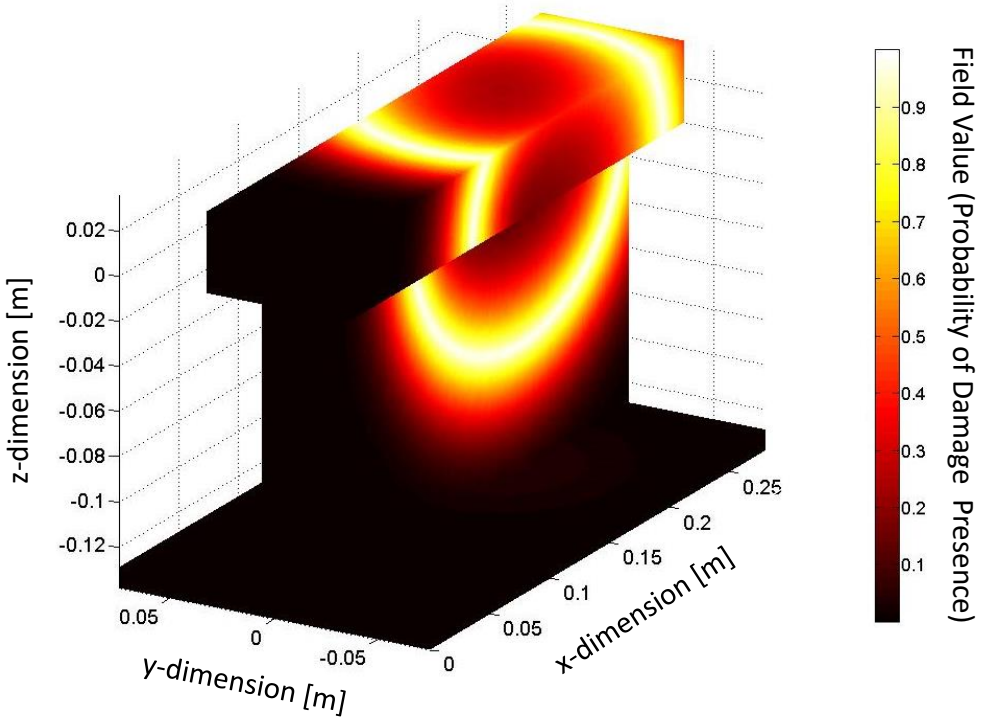
z-dimension [m]
0.02
0
-0.02
-0.04
-0.06
-0.08
-0.1
-0.12
y-dimension [m]
0.05
0
-0.05
x-dimension [m]
0
0.05
0.1
0.15
0.2
0.25
Field Value (Probability of Damage Presence)
0.9
0.8
0.7
0.6
0.5
0.4
0.3
0.2
0.1

(b)

**Figure 9**

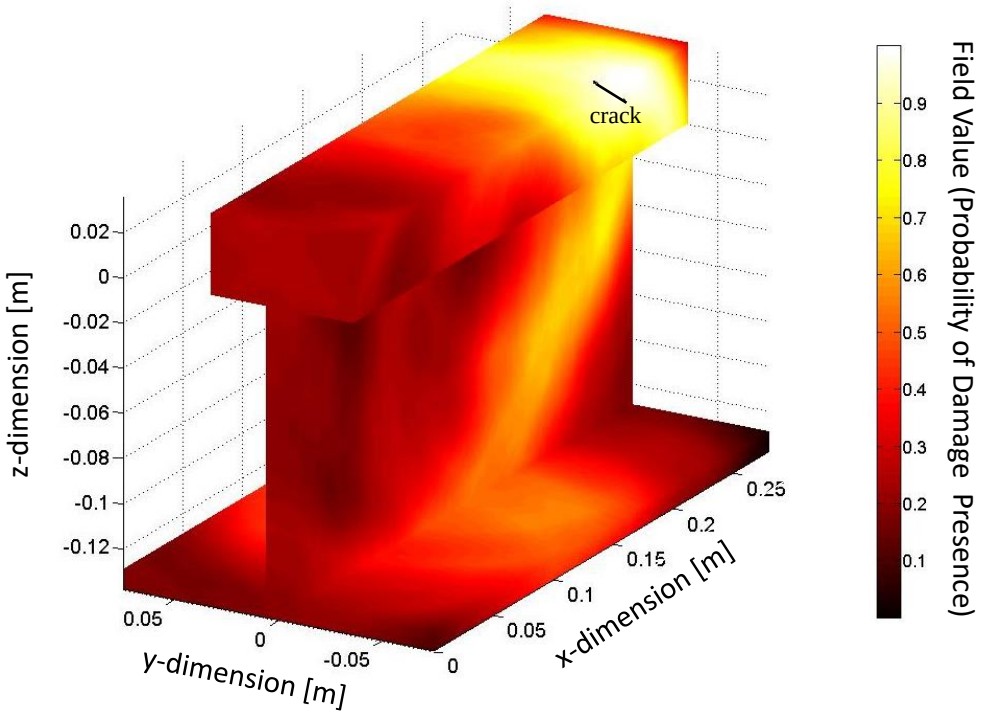
crack
z-dimension [m]
0.02
0
-0.02
-0.04
-0.06
-0.08
-0.1
-0.12
y-dimension [m]
0.05
0
-0.05
x-dimension [m]
0
0.05
0.1
0.15
0.2
0.25
Field Value (Probability of Damage Presence)
0.9
0.8
0.7
0.6
0.5
0.4
0.3
0.2
0.1

(a)

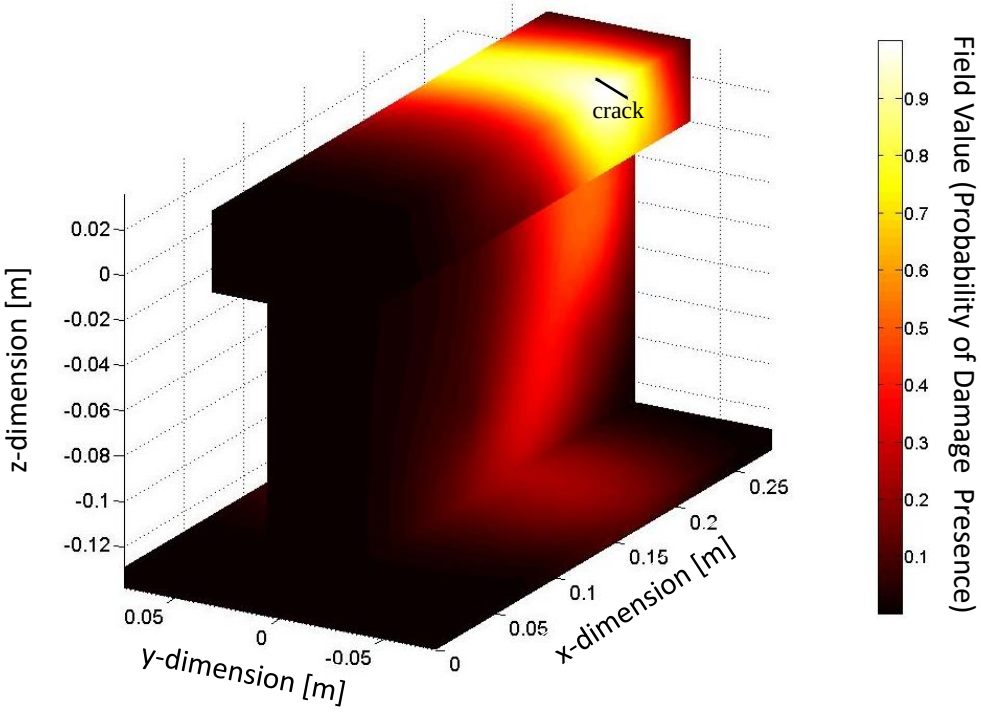
crack
z-dimension [m]
0.02
0
-0.02
-0.04
-0.06
-0.08
-0.1
-0.12
y-dimension [m]
0.05
0
-0.05
x-dimension [m]
0
0.05
0.1
0.15
0.2
0.25
Field Value (Probability of Damage Presence)
0.9
0.8
0.7
0.6
0.5
0.4
0.3
0.2
0.1

(b)

**Figure 10**

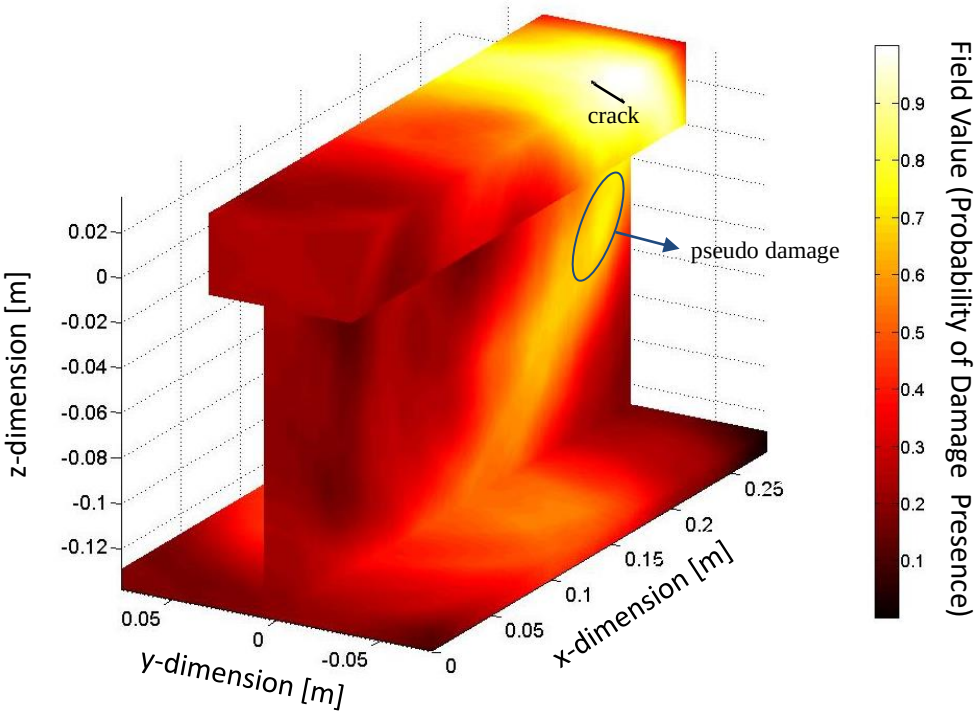
crack
pseudo damage
z-dimension [m]
0.02
0
-0.02
-0.04
-0.06
-0.08
-0.1
-0.12
y-dimension [m]
0.05
0
-0.05
x-dimension [m]
0
0.05
0.1
0.15
0.2
0.25
Field Value (Probability of Damage Presence)
0.9
0.8
0.7
0.6
0.5
0.4
0.3
0.2
0.1

(a)

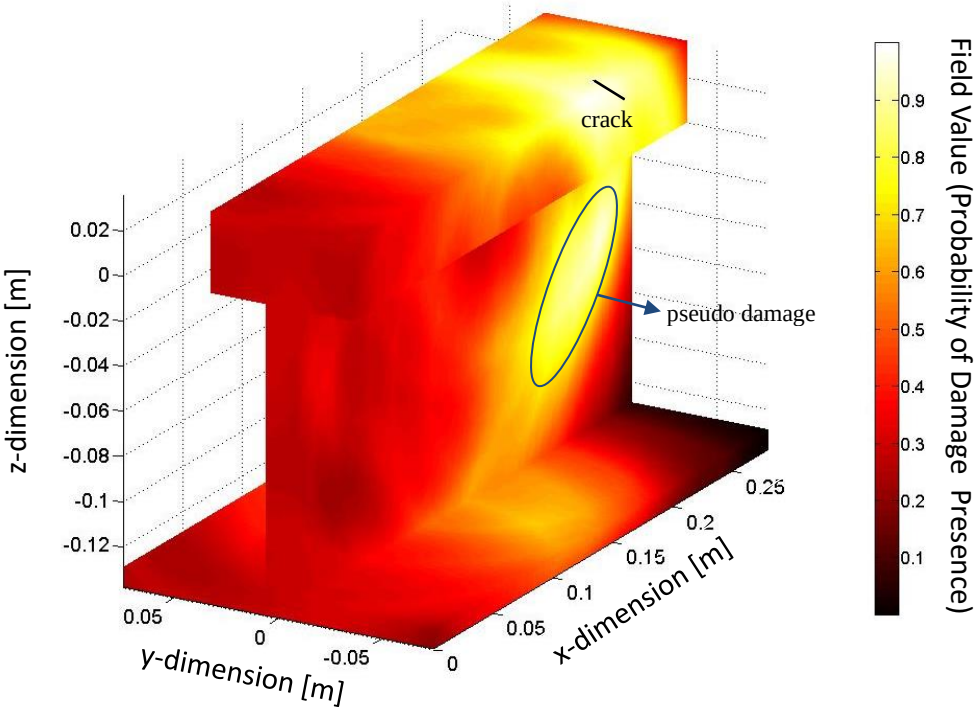
crack
pseudo damage
z-dimension [m]
0.02
0
-0.02
-0.04
-0.06
-0.08
-0.1
-0.12
y-dimension [m]
0.05
0
-0.05
x-dimension [m]
0
0.05
0.1
0.15
0.2
0.25
Field Value (Probability of Damage Presence)
0.9
0.8
0.7
0.6
0.5
0.4
0.3
0.2
0.1

(b)

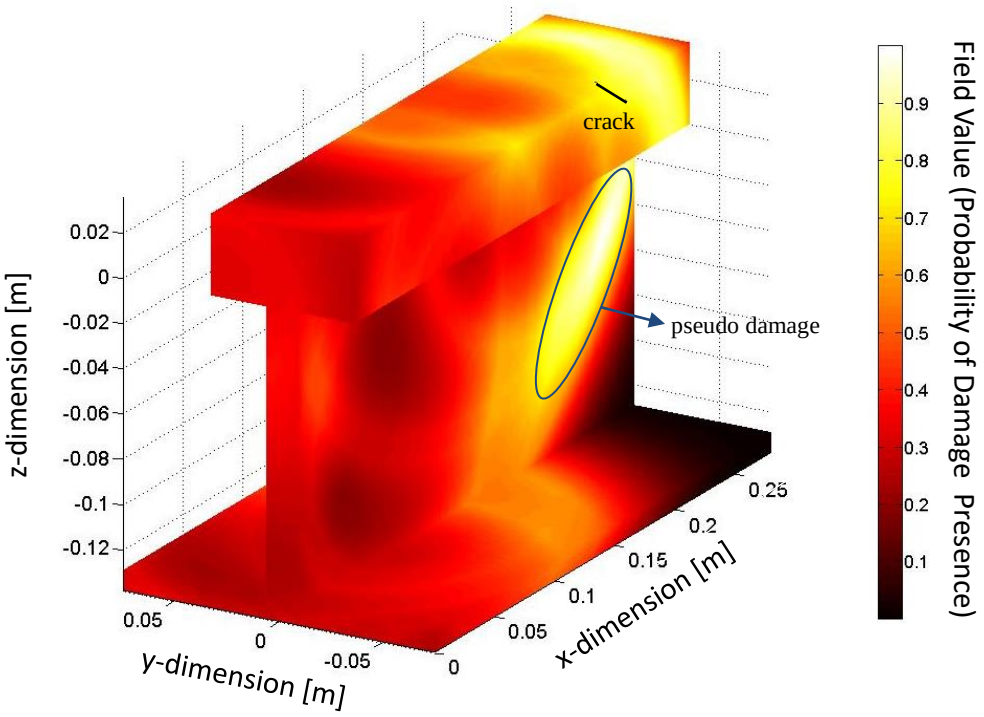
crack
pseudo damage
z-dimension [m]
0.02
0
-0.02
-0.04
-0.06
-0.08
-0.1
-0.12
0.05
0
-0.05
y-dimension [m]
0
0.05
0.1
0.15
0.2
0.25
x-dimension [m]
Field Value (Probability of Damage Presence)
0.9
0.8
0.7
0.6
0.5
0.4
0.3
0.2
0.1

(c)

**Figure 11**

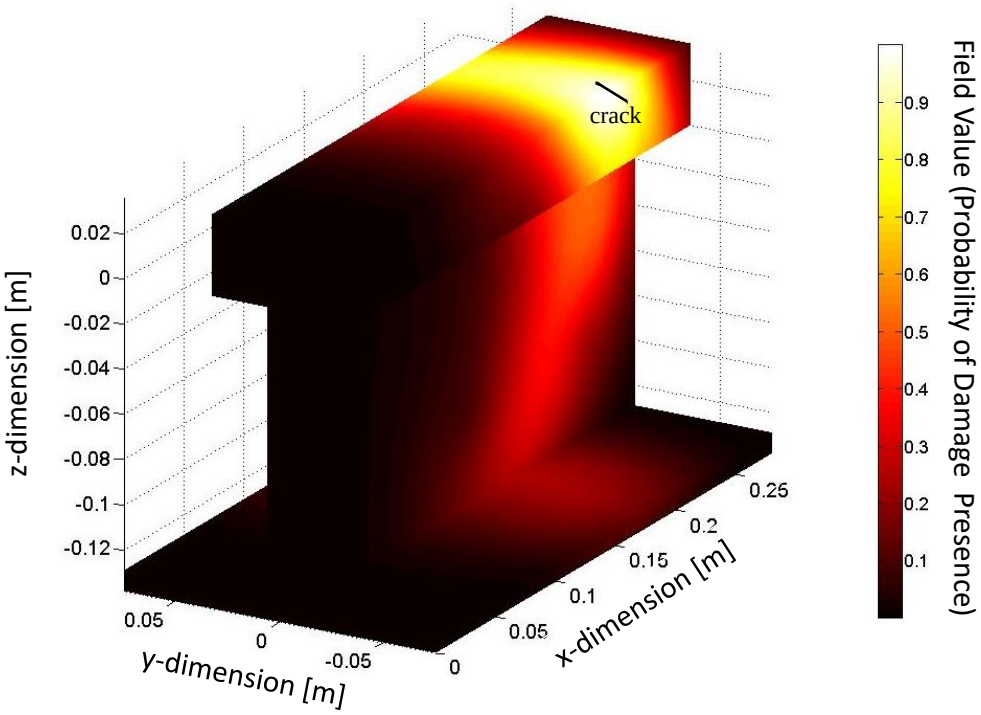
crack
z-dimension [m]
0.02
0
-0.02
-0.04
-0.06
-0.08
-0.1
-0.12
0.05
0
-0.05
y-dimension [m]
0
0.05
0.1
0.15
0.2
0.25
x-dimension [m]
Field Value (Probability of Damage Presence)
0.9
0.8
0.7
0.6
0.5
0.4
0.3
0.2
0.1

(a)

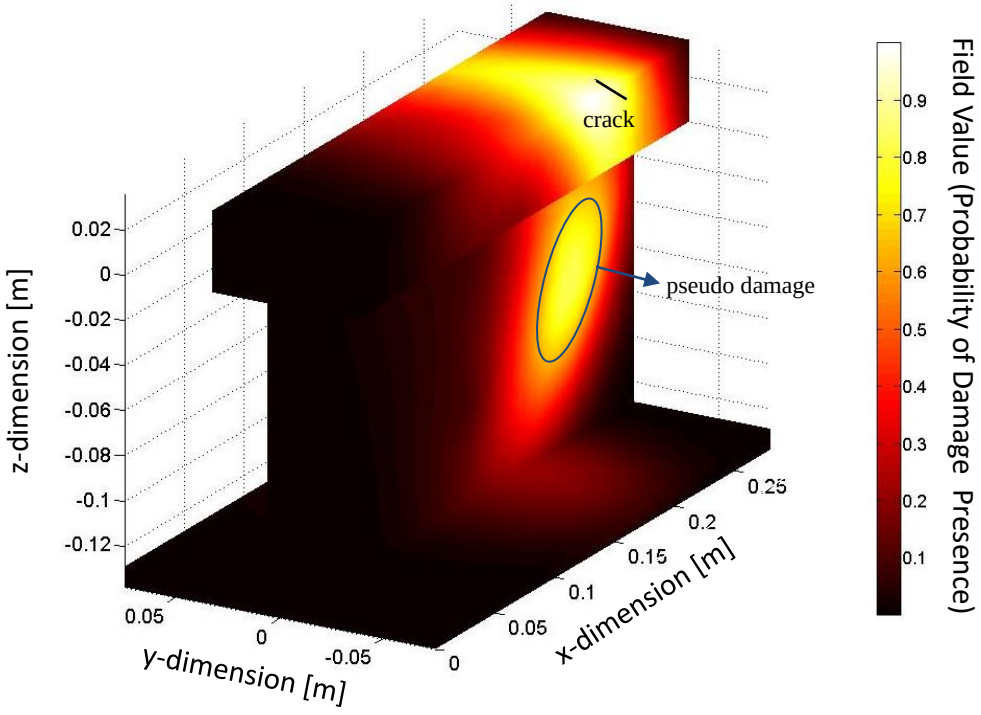
crack
pseudo damage
z-dimension [m]
0.02
0
-0.02
-0.04
-0.06
-0.08
-0.1
-0.12
0.05
0
-0.05
y-dimension [m]
0
0.05
0.1
0.15
0.2
0.25
x-dimension [m]
Field Value (Probability of Damage Presence)
0.9
0.8
0.7
0.6
0.5
0.4
0.3
0.2
0.1

(b)

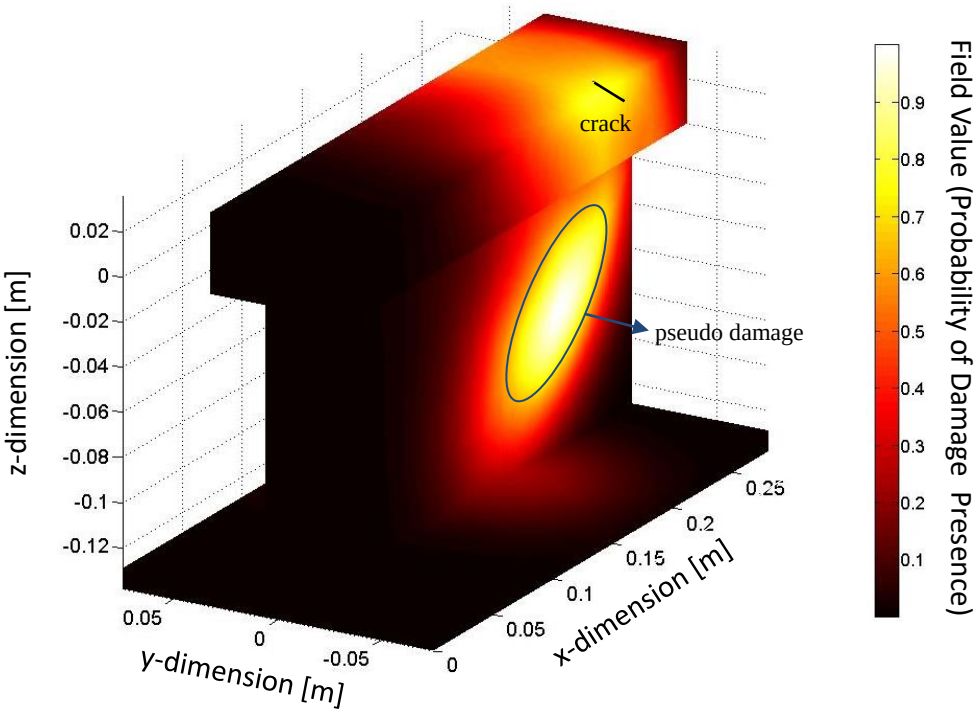
crack
pseudo damage
z-dimension [m]
0.02
0
-0.02
-0.04
-0.06
-0.08
-0.1
-0.12
y-dimension [m]
0.05
0
-0.05
x-dimension [m]
0
0.05
0.1
0.15
0.2
0.25
Field Value (Probability of Damage Presence)
0.9
0.8
0.7
0.6
0.5
0.4
0.3
0.2
0.1

(c)

**Figure 12**

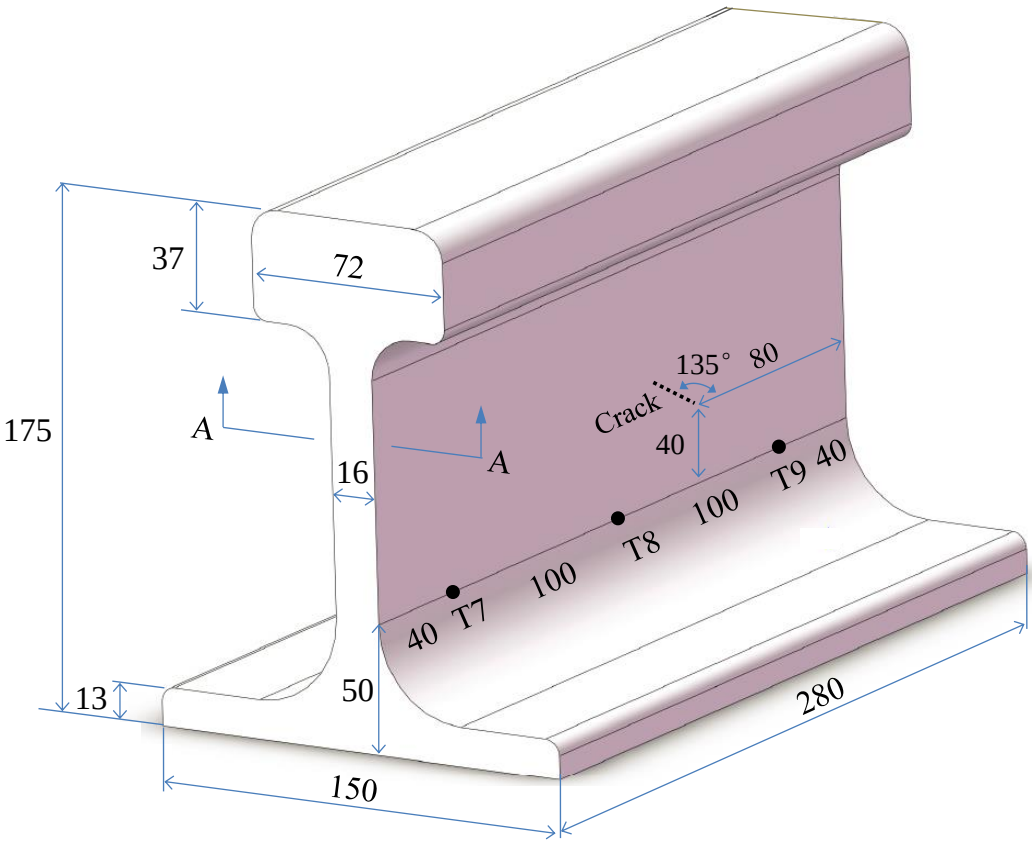


(a)

A—A

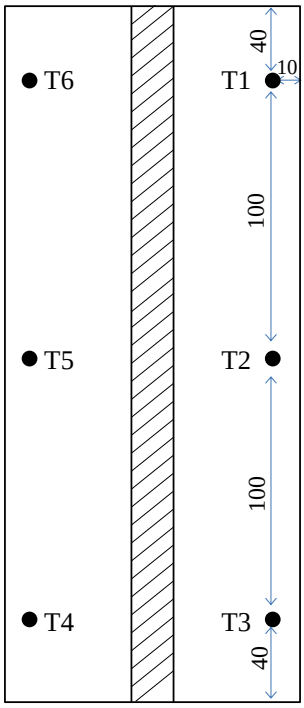


(b)

**Figure 13**

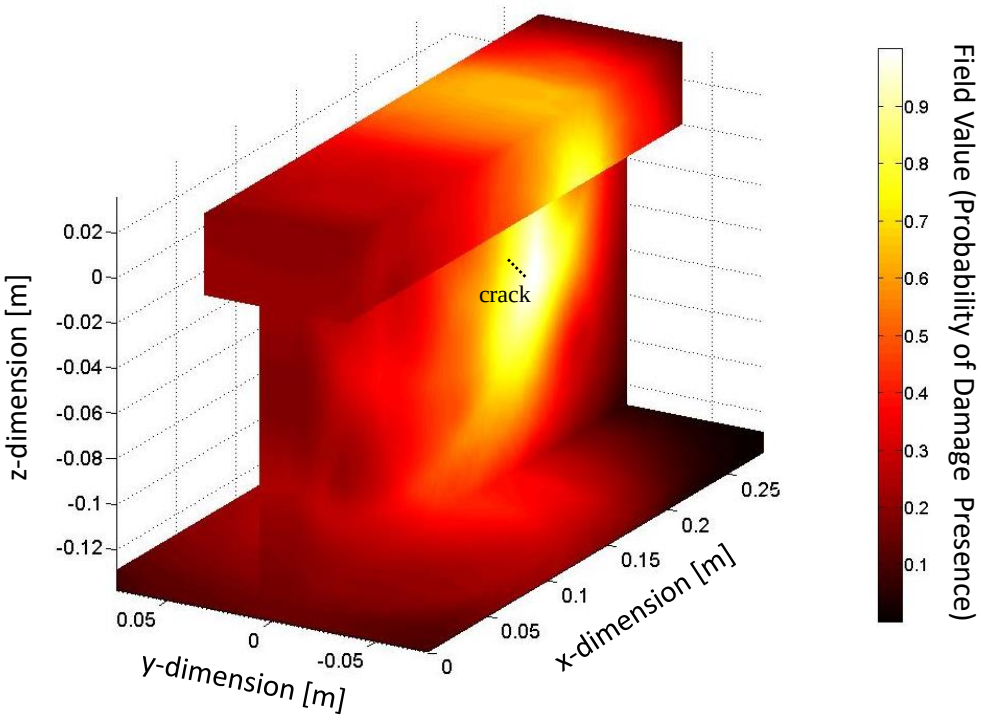
z-dimension [m]
0.02
0
-0.02
-0.04
-0.06
-0.08
-0.1
-0.12
crack
0.05
0
-0.05
y-dimension [m]
0
0.05
0.1
0.15
0.2
0.25
x-dimension [m]
Field Value (Probability of Damage Presence)
0.9
0.8
0.7
0.6
0.5
0.4
0.3
0.2
0.1

(a)

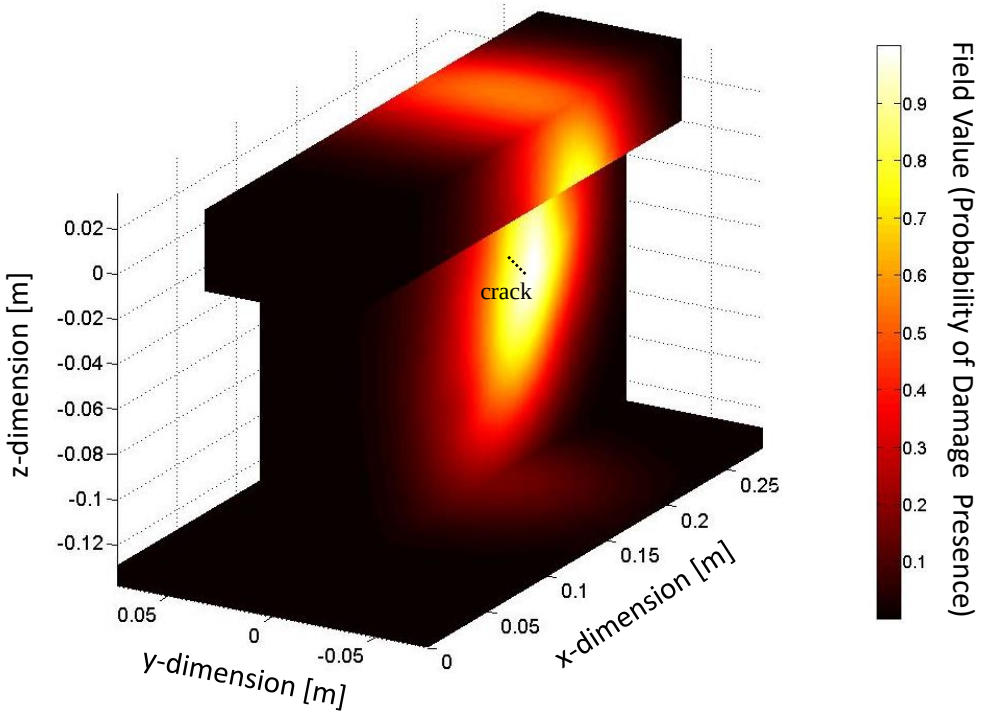
z-dimension [m]
0.02
0
-0.02
-0.04
-0.06
-0.08
-0.1
-0.12
crack
0.05
0
-0.05
y-dimension [m]
0
0.05
0.1
0.15
0.2
0.25
x-dimension [m]
Field Value (Probability of Damage Presence)
0.9
0.8
0.7
0.6
0.5
0.4
0.3
0.2
0.1

(b)

**Figure 14**

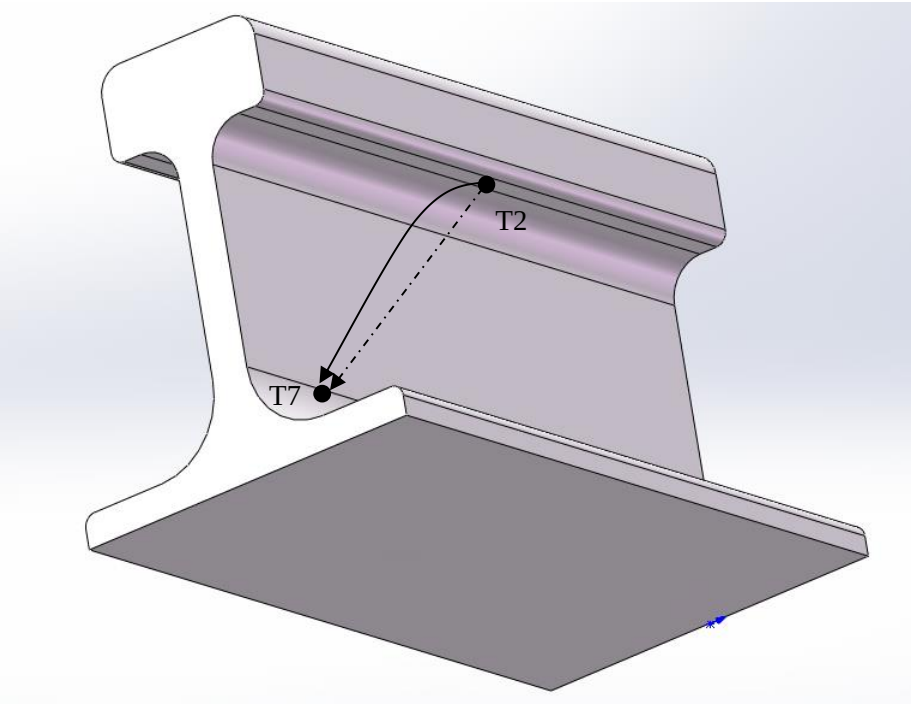


**Figure 15**